Orderly integration of porous TiO$_2$(B) nanosheets into bunchy hierarchical structure for high-rate and ultralong-lifespan lithium-ion batteries

CrossMark

Xiaodan Li[a], Gaoxiang Wu[a], Xin Liu[a], Wei Li[c], Meicheng Li[a,b,*]

[a] *State Key Laboratory of Alternate Electrical Power System with Renewable Energy Sources, North China ElectricPower University, Beijing, 102206, China*
[b] *Chongqing Materials Research Institute, Chongqing 400707, China*
[c] *International Iberian Nanotechnology Laboratory (INL), Braga 4715-330, Portugal*

ARTICLE INFO

ABSTRACT

TiO$_2$(B) has stimulated great interests in lithium storage owing to the highest Li-ion mobility and theoretical capacity among all TiO$_2$ polymorphs. However, the low conductivity and metastability of TiO$_2$(B) still impede its practical application in lithium-ion batteries (LIBs). In this context, the porous TiO$_2$(B) nanosheets offering rich lithium-insertion channels are rational appeals to enhancing the transport kinetics. And the firm 1D TiO$_2$ nanowire can serve as a crossgirder to string together these nanosheets, which improves the deformation resistance of TiO$_2$(B) nanosheets during repeated lithiation/delithiation processes. Herein, the motivation was realized by constructing a bunchy hierarchical structure (TiO$_2$(B)-BH) in a facile solvothermal process. As an anode material for LIBs, TiO$_2$(B)-BH exhibits high reversible capacity, long-term cycling stability (186.6 mA h g^{-1} at 1675 mA g^{-1} after 1000 cycles) and desirable rate performance. The multiple TiO$_2$(B) nanosheets stringed by 1D nanowire possess fast pseudocapacitive behaviour, effective pathway for ion/electron transfer and high structural stability, leading to the superior electrochemical performance of TiO$_2$(B)-BH. This orderly integration strategy of nanosheets can be extendedly applied to the architectural construction of electrode materials for other energy devices.

1. Introduction

Rechargeable lithium-ion batteries (LIBs) are widely used in portable electronic devices owing to their high energy density, wide range of operating temperatures, and long cycle life [1,2]. In the last decades, due to worldwide energy and environmental crises, intensive research efforts have been devoted to developing high power LIBs to meet the increasing demand of electric vehicles and hybrid electric vehicles [3,4]. As one of the crucial components, electrode (especially anode) materials play an important role in the safety and electrochemical performance of high power LIBs [4–7].

Titanium dioxide (TiO$_2$) has been intensively studied as a competitive anode material for high power LIBs due to its excellent cost advantage, safety, and enhanced power capability [8–11]. TiO$_2$ also possesses a relatively high Li ion insertion/extraction potential at 1.5–1.7 V vs. Li$^+$/Li, which does not involve in the decomposition of electrolyte, further ensuring the cycling stability and safety of batteries. Based on the reaction TiO$_2$+xLi$^+$+xe$^-$=Li$_x$TiO$_2$, TiO$_2$ could reversibly storage 0.5–1.0 Li ions per formula unit through an electrochemical reaction path that connects octahedral interstitial sites, thus delivering a theoretical capacity of 168–335 mA h g^{-1} various polymorphs of TiO$_2$

such as anatase [9,12], rutile [11,13], brookite [14], and TiO$_2$(B) [15,16] have been used as anode materials for LIBs application. However, due to the restricted kinetics of solid-state diffusion process, the anatase and rutile exhibit low theoretical capacity of only ~170 mA h g^{-1} [17,18]. In contrast, TiO$_2$(B) possesses an open-channel framework which can provide more insertion sites as well as diffusion paths, combined with a favorable pseudocapacitive lithiation/delithiation behaviour rather than slow solid-state diffusion-controlled lithium storage, thus leading to an enhanced theoretical capacity up to 335 mA h g^{-1} [15,19,20]. However, the poor electronic conductivity of TiO$_2$ materials, especially the increased resistance at the interface between the active electrode and the electrolyte at high current densities still impede the practical application of TiO$_2$(B) in high power LIBs [21–23].

Substantial studies relevant to morphology-dependent performance of anode materials demonstrate that the electrochemical performance of TiO$_2$(B) can be effectively improved by the rational design and controllable synthesis of TiO$_2$(B) materials with unique nano/micro-structures [15,24–26]. Various nanostructured TiO$_2$(B) such as nanoparticles [27], nanotubes [28], nanowires [29], and nanosheets [20] have been explored as anodes owing to kinetically favorable structures

deriving from the large surface areas and reduced sizes. Among them, $TiO_2(B)$ nanosheets growing along the ab plane is found to have high priority on lithium insertion mechanism [20,30], making them to exhibit better electrochemical performance for lithium storage. Particularly, porous $TiO_2(B)$ nanosheets can expose large surface, offering more lithium-insertion channels for fast lithium storage, and the open nanopores can accommodate nanodrops of electrolyte to reduce electrode polarization during high rate charge-discharge [31]. However, $TiO_2(B)$ is a metastable phase of TiO_2 that is prone to irreversible phase transformation into stable phase during the lithiation and delithiation [32], resulting in deficient cycling stability. And the $TiO_2(B)$ nanosheets tend to self-aggregate and become exfoliated upon deep cycling due to the low thermodynamic stability, which deteriorates the conductivity and cycling stability of electrodes. Thus, developing of effective strategies to improve the long-term cyclability of porous $TiO_2(B)$ nanosheets is essential for their applications in LIBs.

Herein, we present a smart assembly strategy to construct TiO_2 bunchy hierarchical structure by integrating porous $TiO_2(B)$ nanosheets onto one-dimensional (1D) TiO_2 nanowire crossgirder. When used as an anode for LIBs, 1D TiO_2 nanowire can provide shortened path for electron/ion transport and prevent the pulverization, aggregation or exfoliation of the nanosheets during repeated lithiation/delithiation processes, thus ensuring the structural integrity of the entire hierarchical system. Meanwhile, the abundant ultrathin $TiO_2(B)$ nanosheets offer high electrode/electrolyte interfacial contact areas, promote rapid charge transfer and pseudocapacitive manners. This proposed porous $TiO_2(B)$ bunchy hierarchical structure enables the $TiO_2(B)$-based anode to exhibit high capacity (278 mA h g^{-1}) and remarkable rate capability (159.2 mA h g^{-1} at 6700 mA g^{-1}), as well as ultra-long lifetime (1000 cycles), demonstrating great potential for practical application.

2. Results and discussion

To achieve fast lithium storage, the porous $TiO_2(B)$ nanosheets with rich lithium-insertion channels are selected as nanoscale building blocks. To get a high structural stability for long-term cycling performance, it is rational to string together the porous $TiO_2(B)$ nanosheets by using a firm TiO_2 nanowire as the crossgirder, constructing $TiO_2(B)$ bunchy hierarchical structure ($TiO_2(B)$-BH). Hence, $TiO_2(B)$-BH will effectively improve the structural stability and fast Li-ion/electron transport, leading to the long-life and high-capacity lithium storage. Here, a facile hydrothermal procedure with Ag cations as the agent and 1D TiO_2 nanowires (Supporting information, Fig. S1a, b) was used for fabrication of such TiO_2 structures, and the schematic processes of which are depicted in Scheme 1. It is obvious that TiO_2 nanowire prepared by the hydrothermal reaction and subsequent calcination is crucial for the construction of bunchy structure, serving as the crossgirder. Without the addition of TiO_2 nanowires, the $TiO_2(B)$ nanosheets tend to aggregate into microspheres in the presence of Ag^+, yielding $TiO_2(B)$-SH (Fig. S1c, d). During above processes, Ag cations play an important role on the formation of $TiO_2(B)$ nanosheets, which could be used to control the morphologies of $TiO_2(B)$-BH (Fig. S2). It is worth noting that a significant difference between $TiO_2(B)$-BH and $TiO_2(B)$-SH is the core size in the centre of hierarchical structures, which is confirmed by the TEM images in Fig. 1b and Fig. S1d. This differential feature may have a strong influence on the electrochemical performance of $TiO_2(B)$ anode.

According to scanning electron microscopy (SEM) image (Fig. 1a), the as-prepared $TiO_2(B)$-BH presents the 3D bunchy structure consisting of abundant ultrathin nanosheets, and the outer diameter is about 2.5 μm. The transmission electron microscope (TEM) further elucidate the detailed feature of $TiO_2(B)$-BH. It is observed that a one-dimensional core existed in the centre of $TiO_2(B)$-BH (Fig. 1b). The size and feature of the core match well with the as-prepared TiO_2 nanowire, indicating the essential role of TiO_2 nanowire in the orderly integrating

of nanosheets. Note that a thick layer (> 1 μm) of TiO_2 nanosheets can be integrated on the 1D long TiO_2 nanowire, which is different from the thin TiO_2 layers (< 100 nm) in previous reports [24,33,34]. In consideration of safe operating window at 1.0–3.0 V, the thicker layer enables a much better load rate and utilization of active material (TiO_2) in electrode. Fig. 1c shows the enlarged shell contrasted from radial oriented nanosheets, and these nanosheets are as thin as several nanometers (Fig. 1b, c). High-resolution TEM (HRTEM) image (Fig. 1d) reveals that the $TiO_2(B)$ nanosheets have nanopores of ca. 5 nm (labelled by white line). The lattice fringes of nanosheets can be clearly observed in Fig. 1e, suggesting a well-defined crystal structure. The fringes with lattice spacing of 0.2 nm, 0.36 nm and 0.58 nm are consistent to (−511), (110) and (200) plane of $TiO_2(B)$ (JCPDS Card No. 35-0088), respectively. Energy-dispersive X-ray spectroscopy (EDX) measurement proves the mainly presence of oxygen and titanium elements in the $TiO_2(B)$-BH (Fig. S3). The corresponding elemental mapping results demonstrate the homogeneous distribution of O and Ti elements in the bunchy structure. There are also small amounts of residual Ag in the $TiO_2(B)$-BH after rinsing. In addition, X-ray diffraction (XRD) pattern of $TiO_2(B)$-BH (Fig. 1f) can be indexed with the $TiO_2(B)$ phase (JCPDS card No. 35-0088), which is in good agreement with the HRTEM observation. All above results demonstrate that multiple porous $TiO_2(B)$ nanosheets are strung together by a firm TiO_2 nanowire and the as-designed $TiO_2(B)$-BH is obtained.

The porous nature of $TiO_2(B)$-BH and $TiO_2(B)$-SH were further characterized by combined nitrogen adsorption-desorption isotherms, as shown in Fig. 2. The adsorption isotherm of $TiO_2(B)$-BH (Fig. 2a) can be classified as a type-IV curve with a H3 hysteresis loop, indicating the presence of slit-like pores composed of $TiO_2(B)$ nanosheets [35,36]. The corresponding BJH pore size distribution calculated from the adsorption branch is presented as the inset. The first peak at the value of 5 nm is due to the pore on the nanosheets, which is consistent with the observation of TEM. And the peak at about 25 nm are related to the interspace between $TiO_2(B)$ nanosheets. The specific surface area and pore volume of $TiO_2(B)$-BH are calculated to be 268 m^2 g^{-1} and 0.95 cm^3 g^{-1}, which are higher than those of $TiO_2(B)$-SH (227 m^2 g^{-1} and 0.67 cm^3 g^{-1}, Fig. 2b). $TiO_2(B)$-BH possess more opened structure than $TiO_2(B)$-SH, especially more interspace between nanosheets, which can be verified by differentiated pore distributions and TEM images. As is well-known, a large surface area could offer high electrode/electrolyte interfacial contact areas, fast Li-ion diffusion and reduced interface resistance, leading to the improved rate capability of $TiO_2(B)$ electrode. In this case, $TiO_2(B)$-BH with large surface area and high pore volume shows great promise in offering sufficient interfacial area for the high rate electrochemical reactions.

$TiO_2(B)$-BH with high structural stability and large surface area was then assembled into Li half-cells to investigate the electrochemical performance. Fig. 3a shows the cyclic voltammetry (CVs) of $TiO_2(B)$-BH electrode at a scan rate of 1.0 mV s^{-1} between 1.0 V and 3 V versus Li^+/Li for the first five discharge/charge cycles. $TiO_2(B)$-BH electrode presents three pairs of redox peaks during the scan process. Two pairs of cathodic/anodic peaks observed in the potential range of 1.4–1.7 V are called S-peaks, which are associated with pseudocapacitive lithium storage behaviour of $TiO_2(B)$ [20]. The small pair of A-peaks at 1.7/ 2.1 V is commonly assigned to the solid-state lithium diffusion in anatase TiO_2 [37]. CV curves with three different scan rate of 0.1, 0.5, and 1 mV s^{-1} were provided to further demonstrate the pseudocapacitive and intercalation behaviour. As shown in Fig. S4a, all the peaks show an increased and broadened trend at high scan rate. Particularly, the increase of S-peaks is much more than that of A-peaks, indicating that pseudocapacitive behaviour increasingly dominated the lithium storage in $TiO_2(B)$-BH with the scan rate increasing. The CV curve of neat TiO_2 nanowires (Fig. S4b) demonstrates an anatase TiO_2 dominated intercalation behaviour at 1.75 V/2.1 V. Hence, it is suggested that TiO_2 nanowire core contribute to the most intercalation lithium storage and the pseudocapacitive behaviour was mainly derived from

Scheme 1. Illustrations of the distinguishing synthesis process of TiO₂ products .
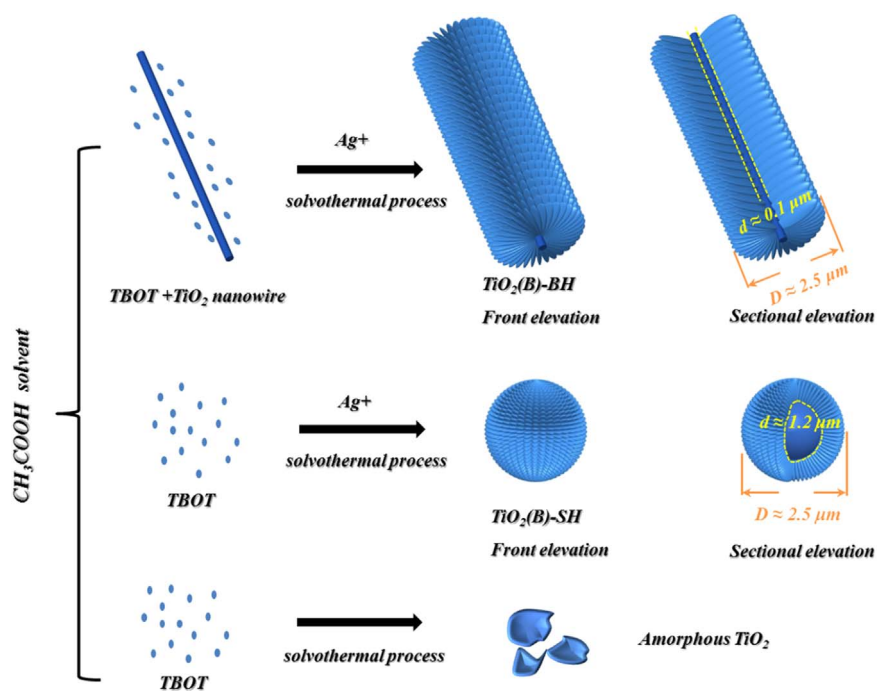
$TiO_2(B)$ nanosheets. Meanwhile, a small amount of $TiO_2(B)$ nanosheets suffer from irreversible phase transition in the synthesis process, transforming into more stable anatase TiO_2. Fig. 3b presents the

Galvano static discharge-charge (GDC) voltage profiles of $TiO_2(B)$-BH electrode in the potential window of 1.0–3.0 V at a current density of 0.25 C (1 C=335 mA g^{-1}). Upon initial discharge, one small voltage
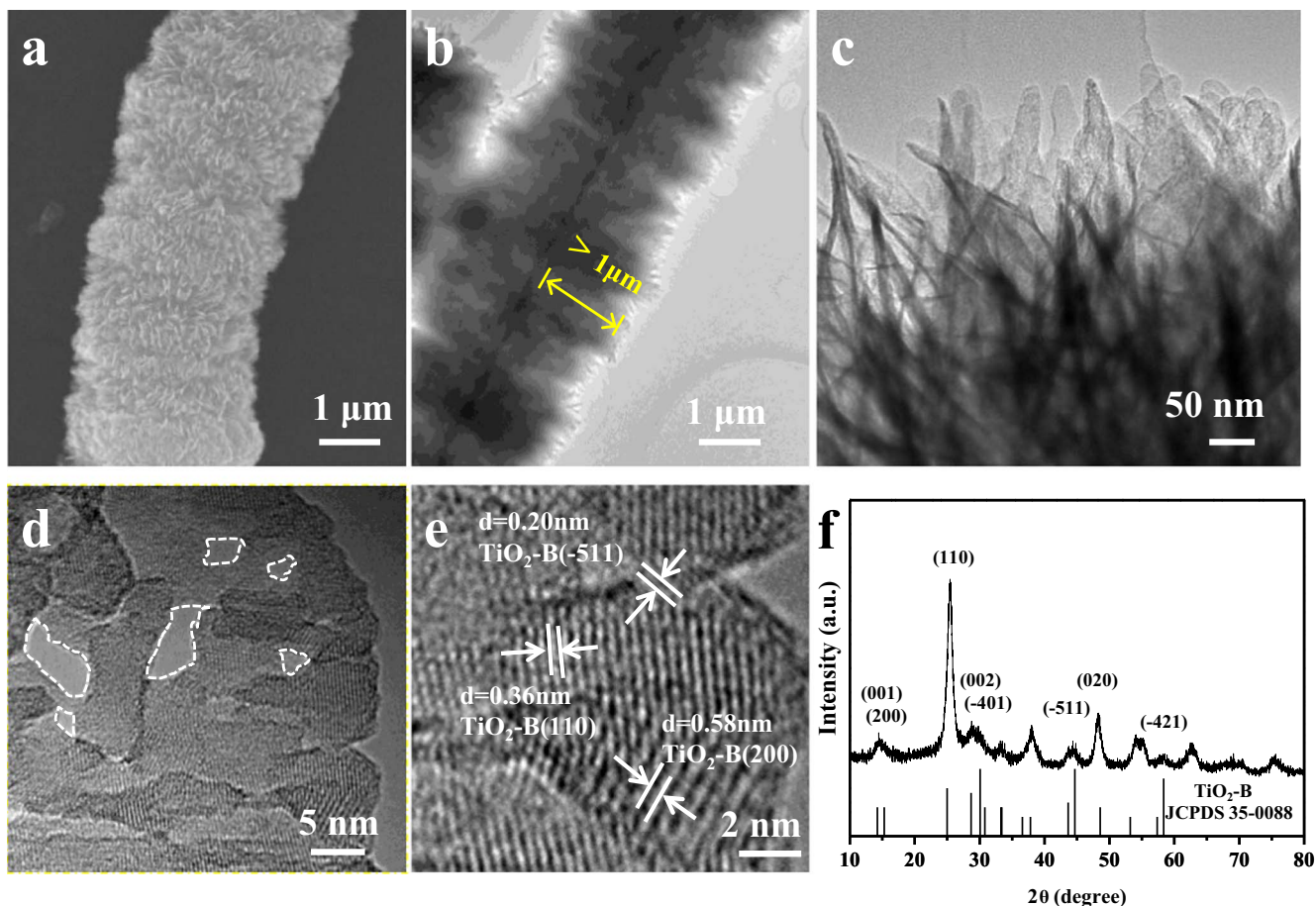
Fig. 1. (a) SEM image of $TiO_2(B)$-BH; (b, c) TEM images of $TiO_2(B)$-BH; (d, e) HRTEM images of TiO_2 nanosheets over the surface of $TiO_2(B)$-BH; (f) XRD pattern of $TiO_2(B)$-BH and standard JCPDS card of $TiO_2(B)$.
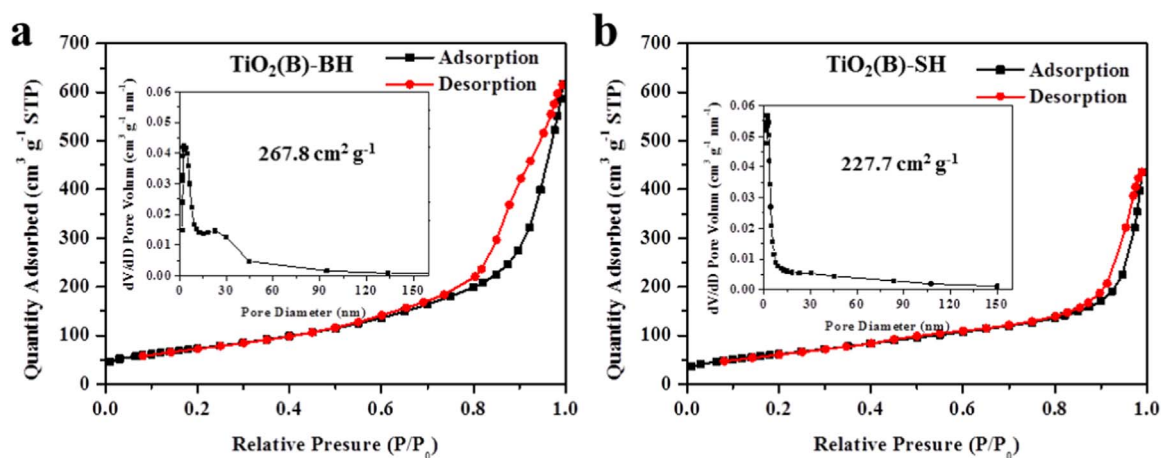
Fig. 2. Adsorption-desorption isotherms of (a) TiO$_2$(B)-BH and (b) TiO$_2$(B)-SH. Insets are their corresponding pore size distribution curves derived from 0 nm to 150 nm.
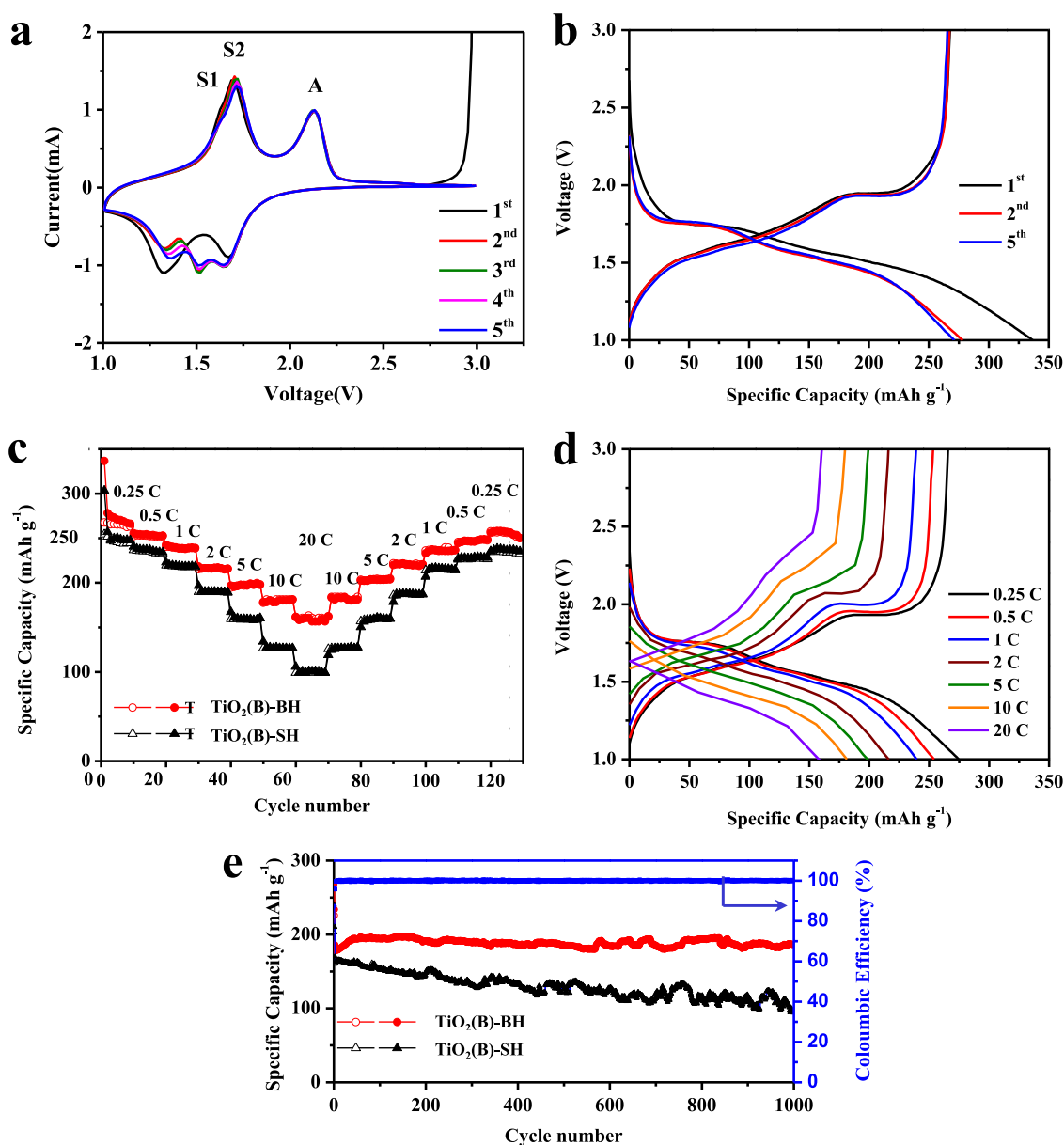

Fig. 3. Electrochemical performance of TiO$_2$(B) hierarchical architectures assembled by nanosheets: (a) Representative CV curves of TiO$_2$(B)-BH for the 1st, 2nd, 3rd, 4th and 5th cycle at a scan rate of 1.0 mV s^{-1}; (b) The charge–discharge voltage profiles of TiO$_2$(B)-BH at a current rate of 0.25 C for 5 cycles; (c) Comparative rate performance of TiO$_2$(B)-BH and TiO$_2$(B)-SH at different current densities; (d) The charge–discharge voltage profiles of TiO$_2$(B)-BH at different current densities; (e) Comparative cycle performance of TiO$_2$(B)-BH and TiO$_2$(B)-SH at current density of C/4 for the first, C/2 for the second and 5 C for the rest cycles.

platform at 1.75 V are attributed to the lithiation of anatase TiO_2, while the long sloped profile from 1.7 to 1.0 V corresponds to pseudocapacitance and surface reactions of TiO_2-B phase. These GDC results are in good accordance with the CV results. Furthermore, the initial discharge and charge specific capacities of $TiO_2(B)$-BH are 337 and 268 mA h g^{-1}, respectively, leading to an initial Coulombic efficiency (CE) of 80%. The initial irreversible capacity loss is mainly ascribed to the interfacial reaction between electrolyte and the active substance on/in $TiO_2(B)$, such as inevitable oxygen, water or active impurity. From the second cycle onwards, the CE of $TiO_2(B)$-BH electrode quickly stabilizes at about 98%.

$TiO_2(B)$-BH electrode also exhibits outstanding cycling performance at varying current densities from 0.25 C to 20 C (1 C=335 mA g^{-1}). As shown in Fig. 3c, the specific discharge capacities are about 278, 254, 239, 217, 198, 180 and 159 mA h g^{-1} corresponding to the current rates of 0.25, 0.5, 1, 2, 5, 10 and 20 C, respectively. For comparison, the rate capacity of $TiO_2(B)$-SH is also tested under the same conditions. Obviously, the specific capacity of $TiO_2(B)$-BH electrode at each rate is much higher than that of $TiO_2(B)$-SH electrode, indicating more effective transport for electron and improved ion adsorption/diffusion kinetics due to the unique structural advantage of $TiO_2(B)$-BH. Comparison performance of TiO_2 nanowires and $TiO_2(B)$-BH was also given in Fig. S5. Obviously, neat TiO_2 nanowires deliver much lower specific capacity than $TiO_2(B)$-BH, indicating the contribution of porous $TiO_2(B)$ nanosheets to high capacity. Fig. 3d displays the corresponding discharge/charge profiles of $TiO_2(B)$-BH electrode at different rates in the voltage range of 1.0–3.0 V. Upon gradually elevating the current density, the long sloped profile remain stably dominates the electrochemical process while the voltage platform fades away. Thus the capacity of $TiO_2(B)$-BH electrode are derived from the fast pseudocapacitive storage at high current rates. These results demonstrate that multiple porous $TiO_2(B)$ nanosheets offered high electrode/electrolyte interfacial contact areas, shortened diffusion path and favorable pseudocapacitive manners, thus contributed to a high specific capacity of $TiO_2(B)$-BH.

To further investigate the cycle stability of the as-prepared samples as anode materials for lithium ion battery, long-term cycling tests of $TiO_2(B)$-BH and $TiO_2(B)$-SH at a high current density of 5 C (1675 mA g^{-1}) were conducted from the 3rd cycle to 10,001,000th cycle (Fig. 3e). A temporary increase of discharge capacity at the first dozens of cycles at 5 C may be caused by the activation process of the porous electrodes, which is common when the charge/discharge process is conducted at high current densities. The capacity profiles of $TiO_2(B)$-BH keep near flat throughout the cycling while $TiO_2(B)$-SH exhibits obvious capacity fading. Specifically, the specific capacity of $TiO_2(B)$-BH keeps from 186.2 mA h g^{-1} to 186.8 mA h g^{-1} at 5 C during 1000 cycles, leading to a capacity retention as high as 100%. As for the $TiO_2(B)$-SH electrode, the initial specific capacity is 169.8 mA h g^{-1} at 5 C and the capacity declines to 95.1 mA h g^{-1} with 56% remained after 1000 cycles. Compared to $TiO_2(B)$-SH, $TiO_2(B)$-BH electrode presents an extraordinary long-term stability, indicating higher structural stability benefited from the unique structure.

Electrochemical impedance spectra (EIS) (Fig. 4) measurements were carried out to further understand the change of $TiO_2(B)$-BH and $TiO_2(B)$-SH electrodes after 1000 cycling tests. A whole Nyquist plot is composed of one semicircle at the high and medium frequency zone, followed by a slope line at the low frequency region. The high-frequency zone is a representation of contact resistance (R_f), and the medium frequency semicircular can be explained as the charge-transfer resistance (R_{ct}) of the electrode/electrolyte interface, while the low-frequency sloping straight line is equivalent to the Warburg impedance (Z_w), corresponding to the diffusion of lithium ions in the electrode. R_e represents the sum of resistances within the bulk electrodes. Therefore, an equivalent circuit can be proposed to analyse the impendence spectra [38], as shown in Fig. 4 insets. The fitting results are displayed in Table 1. Before cycling, the two samples have similar R_e but

differential R_f and R_{ct}. $TiO_2(B)$-BH has a larger R_f resistance compared with $TiO_2(B)$-SH due to more interface resistance caused by the higher surface area of $TiO_2(B)$-BH. On the other hand, the higher surface area could result in a smaller R_{ct} of $TiO_2(B)$-BH, attributing to the plentiful sites for lithium insertion/extraction. After 1000 cycles, $TiO_2(B)$-SH electrode exhibits much larger resistances (R_e, R_s and R_{ct}) compared with $TiO_2(B)$-BH electrode, which is attributed to the pulverization and uneven aggregation occurred inside the $TiO_2(B)$-SH electrode. Furthermore, the high structure stability of TiO_2-BH anode (Fig. 5b) during long-term insertion/extraction of lithium ion enables the formation of stable SEI on its surface, which leads to much lower resistance of TiO_2-BH anode than that of TiO_2-SH anode. Therefore, $TiO_2(B)$-BH electrode demonstrates enhanced kinetic performance, cycling stability and improved conductivity, highlighting significant integration of porous $TiO_2(B)$ nanosheets into bunchy hierarchical structure.

The structure and morphology of $TiO_2(B)$-SH and $TiO_2(B)$-BH were further characterized by TEM after 1000 cycles, as displayed in Fig. 5a, b. The different results are attributed to the influence of the distinguishing cores of $TiO_2(B)$-SH and $TiO_2(B)$-BH (Fig. 5c). In the formation process of $TiO_2(B)$-BH, the as-prepared TiO_2 nanowires serve as cores for the direct growth of $TiO_2(B)$ nanosheets. For the $TiO_2(B)$-SH formed without the assistance of TiO_2 nanowires, the formation process is the development of $TiO_2(B)$ qusi-sphere cores followed by the growth of $TiO_2(B)$ nanosheets on their surfaces. Thus, the core of $TiO_2(B)$-BH is the as-prepared 1D nanowire while the one of $TiO_2(B)$-SH is a self-formed qusi-sphere. In terms of electron transfer, the 1D nanowire provides much better pathways than the qusi-spheres, as shown in Fig. 5c. On the other hand, $TiO_2(B)$-BH is mainly composed by porous $TiO_2(B)$ nanosheets, which provides plentiful lithium insertion channels. Under the circumstances, the thin and flexible TiO_2 nanowire cores in the centre of $TiO_2(B)$-BH are hardly damaged and thus retain intact the bunchy hierarchical structure during repeated lithiation/delithiation (Fig. 5b). While $TiO_2(B)$-SH contains a large qusi-sphere core and a relatively thin nanosheets-shell, which makes lithium easily intercalated into qusi-sphere core. During the long-term discharge/charge process, the solid $TiO_2(B)$ qusi-sphere core would be damaged by the stress of volume changes and TiO_2 nanosheets would peel from $TiO_2(B)$-SH (Fig. 5a). The schematic illustrations of $TiO_2(B)$-SH and $TiO_2(B)$-BH evolution upon cycling are given (Fig. 5c). It is proposed that the bunchy hierarchical structure can well withstand the long-term insertion/extraction of lithium ion, maintaining high structural stability and effective electrical contact inside the electrode, thus $TiO_2(B)$-BH exhibits prominent long-term cycling performance (Fig. 4e).

To clearly demonstrate the superior performance of the as-design $TiO_2(B)$-BH in lithium ion storage, we summarized the electrochemical performance of many representative TiO_2 anodes reported recently in Fig. S4. Our $TiO_2(B)$-BH electrode displays better Li$^+$ storage performance than most TiO_2 materials, including mesoporous $TiO_2(B)$, hierarchical tubular $TiO_2(B)$, $TiO_2(B)$ nanotubes, anatase nanodisks and anatase nanowires. Especially, the high-rate performance and long-term cyclability are desirable due to the porous nature and high structure stability of well-designed $TiO_2(B)$-BH. Firstly, the porous $TiO_2(B)$ nanosheets could provide fast pseudocapacitive behaviour, mass electrode/electrolyte interphase, shortened Li-ion diffusion path and promoted charge transfer. Secondly, the 1D long TiO_2 nanowire cores can afford high-efficiency electron transfer, which leads to a higher electrochemical reactivity and reversibility. Thirdly, the flexible TiO_2 nanowire and its affinity with $TiO_2(B)$ nanosheets contribute to the structural stability of hierarchical system upon lithiation/delithiation. Therefore, $TiO_2(B)$-BH shows promising application for LIBs with high-rate performances and long-term stability. In contrast, $TiO_2(B)$-SH shows a low reactivity and poor structural stability. During a long-term charge/discharge, TiO_2 nanosheets would exfoliate from the surface of qusi-sphere cores, and the hierarchical structure eventually
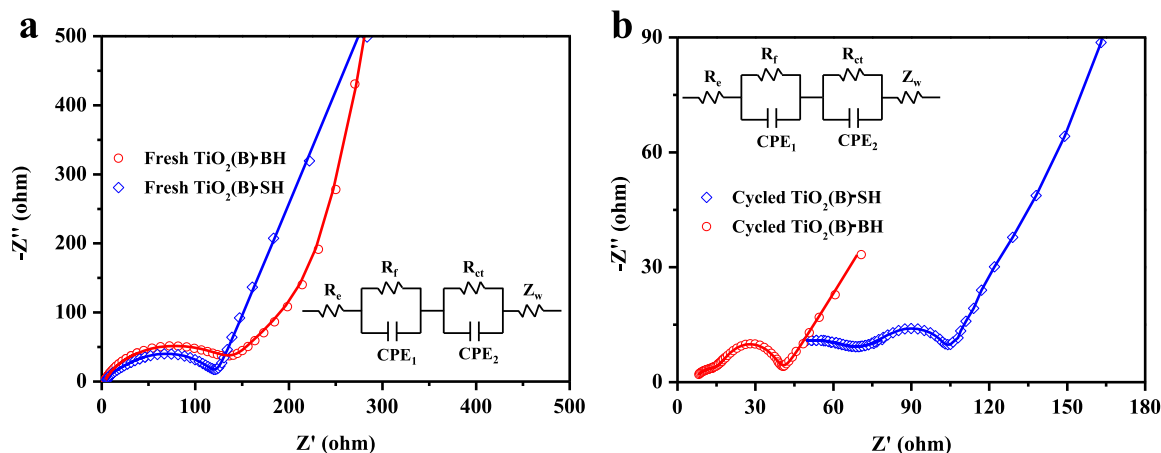
Fig. 4. EIS of TiO$_2$(B)-BH and TiO$_2$(B)-SH: (a) before cycling; (b) after 1000 cycles.

Table 1
Kinetic parameters of TiO$_2$(B)-BH and TiO$_2$(B)-SH electrodes before and after cycling.

Samples	R$_e$ (Ω)	R$_f$ (Ω)	R$_{ct}$ (Ω)
Fresh TiO$_2$(B)-SH	4.80	15.03	101.4
Fresh TiO$_2$(B)-BH	3.05	139.5	85.45
Cycled TiO$_2$(B)-SH	27.26	32.24	44.96
Cycled TiO$_2$(B)-BH	5.94	21.67	11.33

collapses.

3. Conclusions

In summary, the porous TiO$_2$(B) nanosheets indeed can self-assemble into a sphe ral hierarchical structure (TiO$_2$(B)-SH), which delivers specific capacity of 246 mA h g^{-1} (at 0.25 C). In order to achieve higher capacity and better cyclability, we use as-prepared TiO$_2$ nanowire to string together the porous TiO$_2$(B) nanosheets, obtaining a bunchy hierarchical structure (TiO$_2$(B)-BH). Compared with TiO$_2$(B)-SH, the core of TiO$_2$(B)-BH is the as-prepared 1D nanowire rather than a self-formed qusi-sphere. The 1D nanowire core occupies much smaller solid volumes of hierarchical system than the qusi-sphere one, which shortens the electron/ion pathways, decreases the volume changes during lithium insertion/extraction and enhances the structural stability of TiO$_2$(B) hierarchical structure. Meanwhile, the proposed TiO$_2$(B)-BH processes large surface area, high porosity and fast pseudocapacitive behaviour, thereby leading to highly reversible capacities of 278 mA h g^{-1} (at 0.25 C), excellent cycling stability (100% retention after 1000 cycles) and superior rate performance. This integration strategy of nanosize building blocks is a "Goldilocks" principle for the rational design of nanostructured materials for Na/Mg-ion batteries, Li-S batteries and supercapacitors.

4. Experimental section

4.1. Materials synthesis

4.1.1. Chemicals

Titanium dioxide (P25), sodium hydroxide (NaOH), hydrochloric acid (HCl), AgNO$_3$, tetrabutyl titanate (TBOT) and acetic acid (C$_2$H$_4$O$_2$) were purchased from Sigma-Aldrich. All chemicals were used as received without further purification.

4.1.2. Preparation of TiO$_2$ nanowires

2g of TiO$_2$ powder (P25) was mixed with 200 mL of 10 M NaOH aqueous solution. The mixture solution was stirred and then transferred into a Teflon-lined stainless steel autoclave and heated at 180 °C

for 24 h, followed by natural cooling to room temperature. The obtained Na$_2$Ti$_3$O$_7$ powders were washed thoroughly with deionized water followed by a filtration process and dried at 70 °C. The obtained powders were soaked in 0.1 M HCl aqueous solution for 24 h. Finally, the product was separated from the solution by centrifugation, washed with deionized water to the neutral pH, and dried at 70 °C for 10 h. TiO$_2$ nanowires were obtained by calcinating the as-prepared powders at 500 °C in air for 2 h with a heating rate of 10 °C min^{-1}.

4.1.3. Preparation of TiO$_2$(B) bunchy hierarchical structure

In a typical synthesis, 0.02g of TiO$_2$ nanowires were firstly dispersed into 40 mL of acetic acid. Then, TBOT (1 mL) and AgNO$_3$ (0.2g) were added in sequence. After stirring, the mixture solution was transferred into 50 mL Teflon-lined stainless steel autoclaves and heated at 150 °C for 10 h, followed by natural cooling to room temperature. The resulting precipitates were rinsed with deionized water and separated by centrifugation and dried at 60 °C for 12 h under vacuum. The hydrothermal products were further annealed at 350 °C in air for 2 h at a heating rate of 10 °C min^{-1}. The final product of TiO$_2$(B) bunchy hierarchical structure is denoted as TiO$_2$(B)-BH. For comparison, TiO$_2$(B) spherical hierarchical structure was also prepared according to the similar method, except for the addition of TiO$_2$ nanowires. This control sample is denoted as TiO$_2$(B)-SH.

4.2. Characterization

The distribution, size and morphology of the as-prepared samples were characterized by the scanning electron microscopy (SEM, Hitachi S4800). Transmission electron microscopy (TEM), high-resolution TEM (HRTEM) and high-angle annular dark-field scanning transmission electron microscopy (HAADF-STEM) measurements were conducted on a Philips-FEI Tecnai G2 F20 S-Twin microscope equipped with an energy dispersive X-ray (EDX) spectroscopy detector. The chemical compositions and structures of the as-prepared samples were analyzed by X-ray diffraction (XRD) (Bruker D8 Advance X-ray diffractometer, Cu-Kα radiation λ=0.15406 nm). N$_2$ adsorption-desorption analysis was carried out using a Micromeritics ASAP 2020 HD88. The typical sample weight used was about 200 mg. The outgas condition was set to 240 min at 250 °C under vacuum, and all adsorption-desorption measurements were carried out at 77 K. Brunauer-Emmett-Teller (BET) and Barret-Joyner-Halenda (BJH) analyses were used to determine the surface area, pore volume, and pore size distribution of as-prepared samples.

4.3. Electrochemical measurements

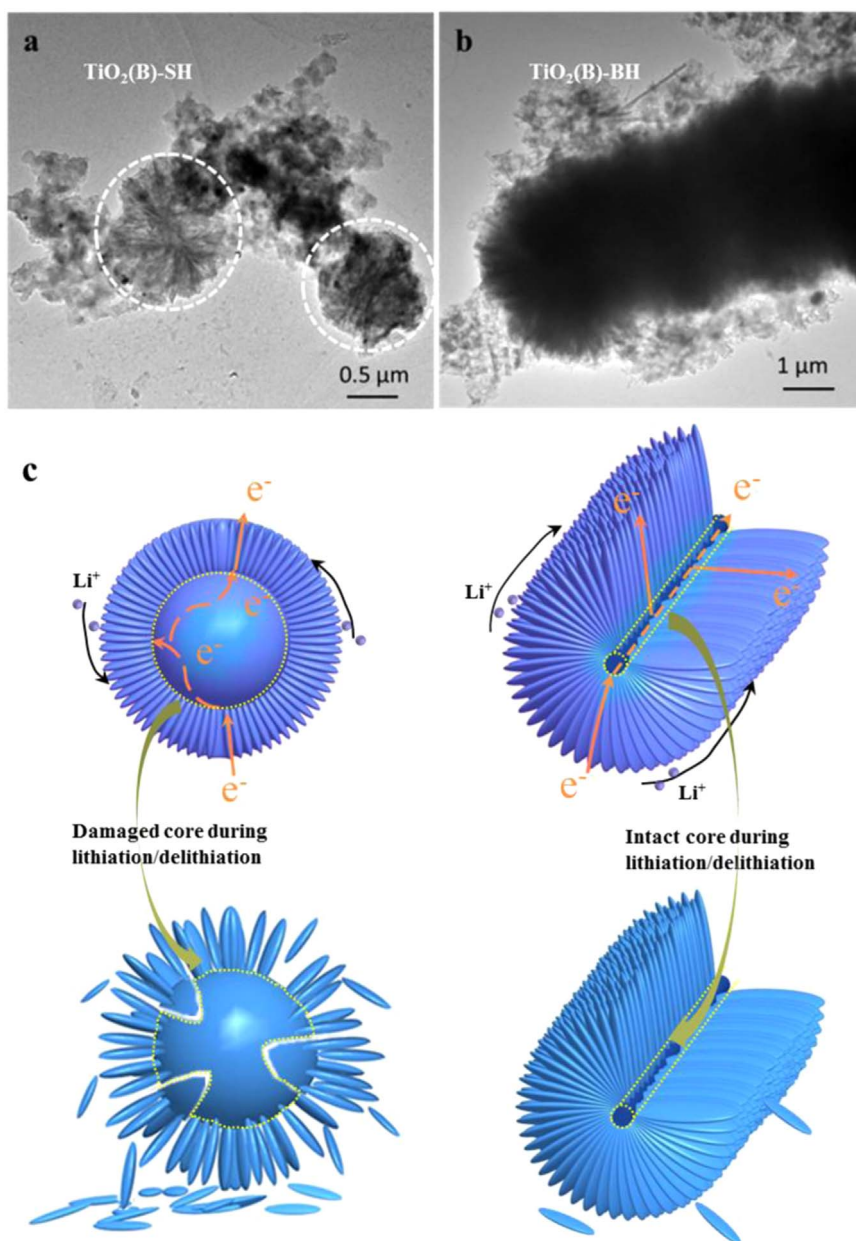The working electrodes were fabricated by coating a slurry contain-

Fig. 5. (a)TEM image of TiO$_2$(B)-SH after 1000 cycles; (b)TEM image of TiO$_2$(B)-BH after 1000 cycles; (c) Schematic illustrations showing the structure evolution of TiO$_2$(B)-SH and TiO$_2$(B)-BH upon cycling, lavender represents lithiation state and blue means delithiation state.

ing 70 wt% of active materials (TiO$_2$(B)-BH, TiO$_2$(B)-SH, or TiO$_2$ nanowires), 20 wt% of acetylene black (Super-P), and 10 wt% of polyvinylidene fluoride (PVDF) dissolved in N-methyl-2-pyrrolidinone (NMP) onto a copper foil and drying at 60 °C for 4 h in vacuum (10^{-3} Torr). Then the sample was dried at 100 °C in vacuum for 12 h before pressing. Standard CR2032-type coin cells were assembled in an Ar-filled glovebox by using the as-prepared anode, Li metal foil (0.6 mm thick) as the counter electrode, and a separator (celgard 2400). The electrolyte was 1 M LiPF$_6$ dissolved in a mixture of ethylene carbonate (EC) and dimethyl carbonate (DMC) (v/v=1:1). The cells were aged for 12 h prior to the electrochemical measurements. Galvanostatic discharge-charge (GDC) experiments were performed at different current densities in the voltage window of 1.00–3.00 V vs Li$^+$/Li with a multichannel battery system (Land, China). Cyclic voltammetry (CV) measurements were conducted on an electrochemical workstation (Zahner Zennium). Electrochemical impedance spectra (EIS) were measured using the same electrochemical workstation by applying an AC voltage of 10 mV amplitude over the frequency range

from 100 kHz to 0.1 Hz. The battery GDC cycling and rate tests were performed with a mass loading of active electrode materials of ca. 0.8–1.0 mg cm^{-2}.

Appendix A. Supporting information

Supplementary data associated with this article can be found in the

online version at doi:10.1016/j.nanoen.2016.11.002.

References

[1] J.M. Tarascon, M. Armand, Nature 414 (2001) 359–367.
[2] B. Scrosati, J. Garche, J. Power Sources 195 (2010) 2419–2430.
[3] M. Armand, J.M. Tarascon, Nature 451 (2008) 652–657.
[4] J.B. Goodenough, Y. Kim, Chem. Mater. 22 (2010) 587–603.
[5] K. Kang, Y.S. Meng, J. Bréger, C.P. Grey, G. Ceder, Science 311 (2006) 977–980.
[6] A.S. Arico, P. Bruce, B. Scrosati, J.-M. Tarascon, W. van Schalkwijk, Nat. Mater. 4 (2005) 366–377.
[7] W. Li, Y.-X. Yin, S. Xin, W.-G. Song, Y.-G. Guo, Energ. Environ. Sci. 5 (2012) 8007–8013.
[8] D. Deng, M.G. Kim, J.Y. Lee, J. Cho, Energ. Environ. Sci. 2 (2009) 818–837.
[9] J.S. Chen, Y.L. Tan, C.M. Li, Y.L. Cheah, D. Luan, S. Madhavi, F.Y.C. Boey, L.A. Archer, X.W. Lou, J. Am. Chem. Soc. 132 (2010) 6124–6130.
[10] D. Wang, D. Choi, J. Li, Z. Yang, Z. Nie, R. Kou, D. Hu, C. Wang, L.V. Saraf, J. Zhang, I.A. Aksay, J. Liu, ACS Nano 3 (2009) 907–914.
[11] Y.S. Hu, L. Kienle, Y.G. Guo, J. Maier, Adv. Mater. 18 (2006) 1421–1426.
[12] C. Kim, R. Buonsanti, R. Yaylian, D.J. Milliron, J. Cabana, Adv. Energy Mater. 3 (2013) 1286–1291.
[13] J. Kong, Y. Wei, C. Zhao, M.Y. Toh, W.A. Yee, D. Zhou, S.L. Phua, Y. Dong, X. Lu, Nanoscale 6 (2014) 4352–4360.
[14] V. Etacheri, J.E. Yourey, B.M. Bartlett, ACS Nano 8 (2014) 1491–1499.
[15] H. Liu, Z. Bi, X.-G. Sun, R.R. Unocic, M.P. Paranthaman, S. Dai, G.M. Brown, Adv. Mater. 23 (2011) 3450–3454.
[16] Y. Ren, Z. Liu, F. Pourpoint, A.R. Armstrong, C.P. Grey, P.G. Bruce, Angew. Chem. Int. Ed. 124 (2012) 2206–2209.
[17] G. Nuspl, K. Yoshizawa, T. Yamabe, J. Mater. Chem. 7 (1997) 2529–2536.
[18] M. Wagemaker, R. van de Krol, A.P.M. Kentgens, A.A. van Well, F.M. Mulder, J. Am. Chem. Soc. 123 (2001) 11454–11461.
[19] M. Zukalová, M. Kalbáč, L. Kavan, I. Exnar, M. Graetzel, Chem. Mater. 17 (2005) 1248–1255.
[20] S. Liu, H. Jia, L. Han, J. Wang, P. Gao, D. Xu, J. Yang, S. Che, Adv. Mater. (24) (2012) 3201–3204.
[21] H.B. Wu, J.S. Chen, H.H. Hng, X. Wen Lou, Nanoscale 4 (2012) 2526–2542.
[22] Q. Wu, J. Xu, X. Yang, F. Lu, S. He, J. Yang, H.J. Fan, M. Wu, Adv. Energy Mater. 5 (2015).
[23] X. Li, W. Li, M. Li, P. Cui, D. Chen, T. Gengenbach, L. Chu, H. Liu, D. Song, J. Mater. Chem. A 3 (2015) 2762–2769.
[24] H. Hu, L. Yu, X. Gao, Z. Lin, X.W. Lou, Energ. Environ. Sci. 8 (2015) 1480–1483.
[25] C. Chen, X. Hu, Z. Wang, X. Xiong, P. Hu, Y. Liu, Y. Huang, Carbon 69 (2014) 302–310.
[26] P. Cui, B. Xie, X. Li, M. Li, Y. Li, Y. Wang, Z. Liu, X. Liu, J. Huang, D. Song, J.M. Mbengue, CrystEngComm 17 (2015) 7930–7937.
[27] C. Wessel, L. Zhao, S. Urban, R. Ostermann, I. Djerdj, B.M. Smarsly, L. Chen, Y.-S. Hu, S. Sallard, Chem. Eur. J. 17 (2011) 775–779.
[28] G. Armstrong, A.R. Armstrong, J. Canales, P.G. Bruce, Chem. Commun. (2005) 2454–2456.
[29] A.R. Armstrong, G. Armstrong, Canales, J.R. García, P.G. Bruce, Adv. Mater. 17 (2005) 862–865.
[30] A.G. Dylla, P. Xiao, G. Henkelman, K.J. Stevenson, J. Phys. Chem. Lett. 3 (2012) 2015–2019.
[31] J. Liu, X.-W. Liu, Adv. Mater. 24 (2012) 4097–4111.
[32] G. Xiang, Y.-G. Wang, J. Li, J. Zhuang, X. Wang, Sci. Rep. 3 (2013) 1411.
[33] H.B. Wu, X.W.D. Lou, H.H. Hng, Chem. Eur. J. 18 (2012) 3132–3135.
[34] S. Liu, Z. Wang, C. Yu, H.B. Wu, G. Wang, Q. Dong, Qiu, J.A. Eychmüller, X.W. Lou, Adv. Mater. 25 (2013) 3462–3467.
[35] S. Brunauer, L.S. Deming, W.E. Deming, E. Teller, J. Am. Chem. Soc. 62 (1940) 1723–1732.
[36] J. Rouquerol, D. Avnir, C.W. Fairbridge, D.H. Everett, J.M. Haynes, N. Pernicone, J.D.F. Ramsay, K.S.W. Sing, K.K. Unger, Pure Appl. Chem. 66 (2009) 1739–1758.
[37] H. Lindström, S. Södergren, A. Solbrand, H. Rensmo, J. Hjelm, A. Hagfeldt, S.-E. Lindquist, J. Phys. Chem. B 101 (1997) 7717–7722.
[38] R. Li, M. Li, Y. Li, P. Fu, Y. Luo, R. Huang, D. Song, J.M. Mbengue, RSC Adv. 5 (2015) 96483–96487.